Received: 21 February 2021 | Revised: 26 April 2021 | Accepted: 28 April 2021

DOI: 10.1002/mrm.28849

FULL PAPER

Magnetic Resonance in Medicine

Sparse precontrast T_1 mapping for high-resolution whole-brain DCE-MRI

Zhibo Zhu[1] | **R. Marc Lebel**[2,3] | **Yannick Bliesener**[1] | **Jay Acharya**[4] | **Richard Frayne**[3,5] | **Krishna S. Nayak**[1,4]

[1]Ming Hsieh Department of Electrical and Computer Engineering, University of Southern California, Los Angeles, California, USA

[2]General Electric Healthcare, Calgary, Alberta, Canada

[3]Radiology and Clinical Neuroscience, Hotchkiss Brain Institute, University of Calgary, Calgary, Alberta, Canada

[4]Department of Radiology, University of Southern California, Los Angeles, California, USA

[5]Seaman Family MR Research Centre, Foothills Medical Centre, Calgary, Alberta, Canada

Correspondence
Zhibo Zhu, Ming Hsieh Department of Electrical and Computer Engineering, University of Southern California 3740 McClintock Ave, EEB 412, Los Angeles, CA 90089-2564, USA.
Email: zhibozhu@usc.edu

Funding information
National Institutes of Health (Grant No. R33-CA225400; principal investigator: Krishna S. Nayak) and the Canadian Cancer Society Research Institute

Purpose: To develop and evaluate an efficient precontrast T_1 mapping technique suitable for quantitative high-resolution whole-brain dynamic contrast-enhanced–magnetic resonance imaging (DCE-MRI).

Methods: Variable flip angle (VFA) T_1 mapping was considered that provides $1 \times 1 \times 2$ mm^3 resolution to match a recent high-resolution whole-brain DCE-MRI protocol. Seven FAs were logarithmically spaced from 1.5° to 15°. T_1 and M_0 maps were estimated using model-based reconstruction. This approach was evaluated using an anatomically realistic brain tumor digital reference object (DRO) with noise-mimicking 3T neuroimaging and fully sampled data acquired from one healthy volunteer. Methods were also applied on fourfold prospectively undersampled VFA data from 13 patients with high-grade gliomas.

Results: T_1-mapping precision decreased with undersampling factor R, although-whereas bias remained small before a critical R. In the noiseless DRO, T_1 bias was <25 ms in white matter (WM) and <11 ms in brain tumor (BT). T_1 standard deviation (SD) was <119.5 ms in WM (coefficient of variation [COV] ~11.0%) and <253.2 ms in BT (COV ~12.7%). In the noisy DRO, T_1 bias was <50 ms in WM and <30 ms in BT. For $R \leq 10$, T_1 SD was <107.1 ms in WM (COV ~9.9%) and <240.9 ms in BT (COV ~12.1%). In the healthy subject, T_1 bias was <30 ms for $R \leq 16$. At $R = 4$, T_1 SD was 171.4 ms (COV ~13.0%). In the prospective brain tumor study, T_1 values were consistent with literature values in WM and BT.

Conclusion: High-resolution whole-brain VFA T_1 mapping is feasible with sparse sampling, supporting its use for quantitative DCE-MRI.

A preliminary version of this work was presented at the International Society for Magnetic Resonance in Medicine 27th Annual Meeting & Exhibition; May 11-16, 2019; Montreal, Quebec, Canada; Abstract #4544.

KEYWORDS
brain tumor, model-based reconstruction, quantitative dynamic contrast-enhanced–magnetic resonance imaging (DCE-MRI), sparse sampling, T_1 mapping

1 | INTRODUCTION

Dynamic contrast-enhanced–magnetic resonance imaging (DCE-MRI) is a powerful imaging tool that can reveal the spatial distribution of vascular parameters, including permeability and plasma volume, through tracer-kinetic (TK) modeling.[1,2] It involves collecting a series of T_1-weighted images during the arrival and passage of a T_1-shortening contrast agent.[3,4] Quantitative DCE-MRI has shown value in diagnosing and monitoring of various brain diseases, including tumors,[5,6] multiple sclerosis,[7,8] and Alzheimer disease.[9]

Widespread clinical application is limited by low spatial resolution, insufficient spatial coverage, and long data acquisition. Recent studies have overcome these limitations using parallel imaging techniques[10,11] and compressed sensing,[12] or model-based reconstruction techniques to simultaneously achieve high spatial resolution and whole-brain coverage. For example, Lebel et al demonstrated a method combining compressed sensing and parallel imaging,[13] which was later validated in patients with brain tumors by Guo et al.[14] Several more recent works have showed the benefits of model-based reconstruction that incorporate the model used for DCE parameter quantification. For example, Dickie et al proposed joint estimation of T_1 and tracer-kinetic maps[15] to improve accuracy and precision. Guo et al developed a direct estimation of tracer-kinetic parameters[16] and a joint estimation with patient-specific arterial input function.[17] Lingala et al used dictionary-based constraints.[18] Most of these previous works either employed fully sampled T_1 mapping, which is not feasible in the clinic, or assumed a fixed T_1 value for brain tissue, which is not realistic.

Precontrast M_0 and T_1 maps with matching spatial resolution and coverage are required for these methods to be practically applied in patients. This can be achieved via variable flip angle (VFA)[19] or inversion recovery (IR)[20] imaging. IR is considered the gold standard for T_1 mapping, and substantial bias exists between VFA and IR. Despite this bias, VFA is the most widely used approach for precontrast T_1 mapping in DCE-MRI because it is faster and acquisition parameters can be precisely matched to the three-dimensional (3D) spoiled gradient recalled echo (SPGR) sequence that is used for the main DCE-MRI scan. However, high-resolution whole-brain full-sampling VFA imaging *may* be impractical because of the long scan time required. This leads to an unmet need for resolution- and coverage-matched rapid precontrast T_1 mapping. Lebel et al showed that T_1 mapping is feasible using sparsely sampled VFA acquisition integrated with DCE-MRI.[21] Maier et al showed sparse T_1 mapping estimation using total variation (TV) and total generalized variation (TGV) constraints[22] in healthy volunteers. Note that the appropriateness of spatial smoothness constraints in patients with brain tumors is unclear because of potential T_1 heterogeneity. These works collectively show the potential value of model-based and/or constrained reconstruction techniques to accelerate VFA T_1 mapping.

In this work, we evaluate a time-efficient direct T_1 mapping approach specifically for high-resolution whole-brain quantitative DCE-MRI in patients with brain tumors. We use a brain tumor digital reference object (DRO) to determine accuracy under both noiseless and 3T-mimicking scenarios. We evaluate the approach in vivo by retrospectively undersampling fully sampled VFA data from a healthy volunteer to identify possible artifacts and image quality issues. Finally, we apply the approach to prospectively undersampled VFA scans to assess heterogeneity of T_1 measurements in patients with high-grade gliomas.

2 | METHODS

2.1 | Variable flip angle T_1 mapping

VFA mapping involves the collection of a series of T_1-weighted SPGR images with different prescribed FAs β_i. VFA imaging is sensitive to B_1^+ inhomogeneity,[23] which requires the acquisition of a B_1^+ scale map (b_1) to estimate actual FAs $\alpha_i = b_1\beta_i$. We use the SPGR steady state signal model that describes signal D_i as a function of M_0, T_1, actual flip angle α_i, and TR:

$$D_i\left(M_0, T_1, \alpha_i\right) = \frac{M_0 \sin\alpha_i \left(1 - E_{10}\right)}{1 - E_{10}\cos\alpha_i} \tag{1}$$

where $E_{10} = e^{-\frac{TR}{T_1}}$. Note that the effect of T_2^* decay is neglected due to short and unchanging TE. Voxel-based pre-contrast M_0 and T_1 values can be efficiently estimated through a SPGR model fitting process:

$$\begin{bmatrix} M_0\left(1-E_{10}\right) \\ E_{10} \end{bmatrix} = A^{\dagger} \begin{bmatrix} D_1 \\ D_2 \\ \vdots \\ D_{N_{FA}} \end{bmatrix} \tag{2}$$

where $A = \left[\sin\alpha_i \; D_i\cos\alpha_i\right]$, as described by Deoni et al.[23,24] Note that M_0 and T_1 are jointly estimated and are, therefore, correlated. In this work, we focus on T_1 accuracy and precision because it is crucial for quantitative DCE-MRI[25,26] and is measured in meaningful physical units. The Appendix A contains an analysis of the impact of a precontrast T_1 mapping error on quantitative DCE-MRI.

2.2 | Sparse T_1 estimation

When VFA data/images are undersampled, it is possible to perform sparse image reconstruction for each FA before T_1 estimation on a voxel-by-voxel basis.[27-29] However, this does not leverage shared information across the images. Alternatively, T_1 mapping can be performed for the entire volume in a single step directly from the undersampled k-space data. This skips the intermediate step of forming images for each FA, and instead relies on accurate forward models. The key benefit is that T_1 information is extracted from the data in an optimal way, from an information-theoretic perspective. Details of the sampling pattern are provided in the Supporting Information and illustrated in Supporting Information Figure S1.

2.3 | Direct T_1 estimation

Direct T_1 estimation can be performed by solving the following inverse problem:

$$\left(M_0, T_1\right) = \min_{M_0, T_1} \frac{1}{2} \left\| F_u S D\left(M_0, T_1, \alpha\right) - d \right\|_{l_2}^2 \qquad (3)$$

Data consistency measures the distance between the forward signal model applied to the estimate and the sampled data at measured locations in (k, FA) space, where F_u is the undersampled Fourier transform operator, S is the coil sensitivity, D is the steady state SPGR forward model including the measured b_1, and d is the measured k-space data. A necessary condition for the problem to be well-posed is that the number of measurements are larger than the number of unknowns, for example, $\frac{N_{FA}\dim(C)}{R} > 2N$, where C is the subspace spanned by coils, N is the number of voxels, and R is the undersampling factor. This indicates that the problem will be ill-posed if $R > \frac{N_{FA}\dim(C)}{2}$. Ideally, $\dim(C)$ is equal to number of coils, N_c, if coils are linearly independent to each other. In this work, the aforementioned problem is solved using the nonlinear conjugate gradient (NCG) method initialized with $M_0 = 0$ and $T_1 = 1000$ ms within the field of view.

2.4 | Evaluation in a digital reference object

An anatomically realistic DRO[30,31] was used to evaluate accuracy and precision of M_0 and T_1 maps as a function of noise level and the undersampling rate. Each healthy tissue type in the DRO was assigned T_1 values based on the literature,[32] for example, 1084 ms for WM, and M_0 values were normalized with respect to cerebrospinal fluid (CSF). To the best of our knowledge, a brain tumor such as a glioma, has T_1 values longer than healthy tissues, with the literature reporting 1392-3601 ms.[33-35] Therefore, we set T_1 to be 2000 ms for BT in the DRO. The DRO has a matrix size of $256 \times 256 \times 12$, matching a spatial resolution of $0.94 \times 0.94 \times 5$ mm^3. Simulated scan settings, for example, FA, pulse repetition time (TR), and echo time (TE), are identical to our in vivo experiment settings, including phase encoding in the axial plane. An eight-channel coil sensitivity map was simulated based on in vivo measurement at 3T MRI scanner (HD23; GE Healthcare). Noise was simulated at a level matching typical 3T MRI at our center, and one order of magnitude lower and higher. Undersampling factors in range from 1× to 40× were considered for the noiseless case. In the noiseless case, for each undersampling factor we considered up to 10 different realizations to account for potential variability in the sampling. For experiments under noise corruption, we considered undersampling factors ranging from 1× to 40×, each factor with one sampling pattern realization and up to 50 noise realizations, which was found enough to stabilize estimation of bias and standard deviation (SD) of T_1 estimates.

Our analysis focused on white matter (WM) and brain tumor (BT) regions of interest (ROIs). T_1 values within these ROI's are reported in histograms for each undersampling factor and/or noise level. We also compare reconstructed T_1 values with the assigned ground truth. Mean and SD of T_1 values are plotted as a function of the undersampling factor, and the coefficient of variation (COV) is computed to numerically reflect the accuracy and precision of the results and their evolution as the undersampling factor increases.

2.5 | In vivo experimental methods

In vivo experiments were performed on a clinical 3T MRI scanner (MR750; GE Healthcare) with a 12-channel head–neck–spine receiver coil. Imaging protocols were approved by the relevant institutional review board; all subjects provided written informed consent. B_1^+ mapping was performed using the Bloch-Siegert approach.[36] Data were acquired with a coronal slab orientation, with superior-inferior as the readout direction. The VFAs were logarithmically spaced from 1.5° to 15°. Acquisition settings: TR = 4.9 ms, TE = 1.9 ms, field of view (FOV) = $240 \times 240 \times 240$ mm^3, slice thickness

= 2 mm, and matrix size = 256 × 240 × 120. The pulse sequence was derived from the vendor product sequence and modified to acquire specific phase encodes and tip angles; the sequence used slab-selective excitations and the RF and gradient spoiling were unchanged.

For the retrospective study (one healthy volunteer, full sampling), the acquisition time was 16 min and 48 s. For the prospective study (13 patients), the acquisition time was 576 s consisting of both T_1 mapping (245 s) and sparse DCE (5 s/frame, contrast injection at ~4 min), and a fully sampled 40 × 40 phase-encoding grid of the k-space center was acquired for FA = 1.5° (8 s of scan time) for coil sensitivity estimation. The coil sensitivity maps were estimated from this image, by dividing the individual-coil low-resolution anatomic images by the coil-combined image. There is also a brief transient approach to steady state every time there is a change in the applied FA. We discarded the first 4.5 seconds for the first FA, and the first 2 seconds for each subsequent FA. This was adequate to ensure spins were within ±7% of their steady-state value for T1s in the range 1300 to 2500 ms.

All reconstructions were performed offline. Tissue masks (eg, WM) for fully sampled healthy volunteer data were extracted using the FMRIB's Automated Segmentation Tool (FAST) toolbox[37] (https://fsl.fmrib.ox.ac.uk/fsl/fslwiki/FAST) using fully sampled images at 10.22°, which had the best gray matter (GM)–WM contrast-to-noise ratio.

2.6 | Evaluation in a healthy adult

Fully sampled VFA measurement was obtained from one healthy adult volunteer (M/26). Raw data were retrospectively subsampled in (k-, FA) space with undersampling factors ranging from 1× to 40×, each with up to 10 realizations of the randomized sampling pattern. Our analysis focused on WM ROIs. Results are reported and analyzed in a similar fashion as for noisy DRO study, except that T_1 maps estimated from fully sampled scans served as reference. In addition, a T_1 spatial map and an absolute fractional difference spatial map were employed to show spatial patterns in T_1 values.

2.7 | Prospective application to patients with brain tumors

Methods were evaluated prospectively in 13 patients with high-grade glioma brain tumor (four males and nine females, age range 42–80 years). These data were acquired between December 2016 and April 2019. The vendor-provided 3D spoiled gradient echo sequence was modified to include sparse VFA sampling with R = 4 before sparse DCE-MRI, as described by Lebel et al.[21] The resulting T_1 maps were qualitatively evaluated by a neuroradiologist for visual quality (noise, tissue inhomogeneity, tissue differential), evidence of tumor, postsurgical cavity, and artifacts. These maps were also given a qualitative score on a three-point Likert scale. The score was defined as follows: 0 = nondiagnostic because of artifacts and/or difficulty visualizing tissue boundaries; 1 = diagnostic, may have mild artifacts, adequate visualization of tissue boundaries; 2 = diagnostic with high quality, no visible artifacts, and well-defined tissue boundaries).

Small ROIs were manually drawn for WM, BT, and temporalis and surgical cavities; mean and SD of T_1 values are reported for these ROIs. The ROIs of the tumor were hand-drawn by a board-certified neuroradiologist with 9 years of experience. They were selected based on the imaging morphology and signal intensity of the tumoral and peritumoral tissue. The selections were based on the assessment of the imaging features, including regional mass effect, volume loss, and findings suggestive of cellular tumor (based on a visual qualitative assessment of the T_1 mapping signal compared with other intracranial structures), which are all findings that are commonly used to assess for neoplasm on conventional MRI sequences.

3 | RESULTS

3.1 | Validation using a digital reference object

Figure 1 shows the results of noiseless and 3T-mimicking noisy DRO cases. Results gathering 10 undersampling realizations and results gathering 50 noise realizations are reported for noiseless and noisy cases, respectively. The SNR level of 50 is chosen for display because it is the closest to our clinical protocol. In Figure 1A,B,E,F histograms of both tissues behave as approximately impulse for $R \leq 10$, and approximately Gaussian for $R \geq 16$ for noiseless cases. In the noisy cases, histograms are approximately Gaussian for $R \leq 10$ and are almost flat for $R \geq 16$. This can be also seen numerically from Figure 1C,D,G,H. As expected, T_1 SD gets monotonically larger with higher undersampling factor. In the noiseless case, when $R \leq 10$ (VFA scan time ≥137.63 s), the T_1 bias is <1 ms and SD is <40 ms for both tissues. In the 3D-mimicking case, when $R \leq 10$, the T_1 bias is <10 ms and SD is <110 ms (WM) and <250 ms (BT), and when $R > 16$, the T_1 mean starts changing randomly and its SD overshoots in BT.

3.2 | Validation in a healthy adult volunteer

Figure 2 shows the results of T_1 mapping using healthy volunteer data. As undersampling increases, the histograms become broader and have thicker tails (Figure 2A). This matches what

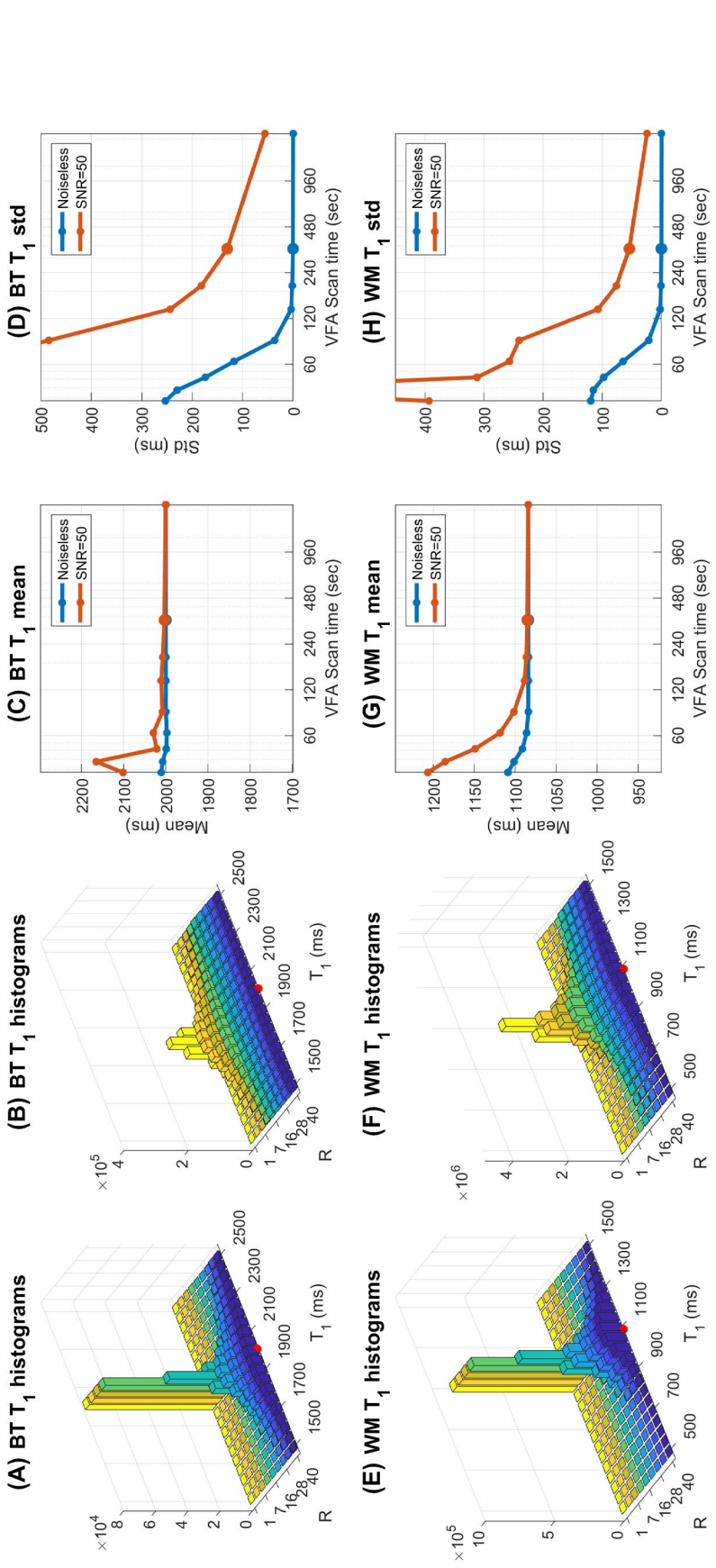

FIGURE 1 Brain tumor digital reference object (DRO) results. A, T_1 histograms for the noiseless DRO. B, T_1 histograms for the 3T-mimicking noisy DRO. C, T_1 mean values. D, T_1 standard deviation (Std) values. All are plotted as a function of (A,B,E,F) undersampling factor or (C,D,G,H) variable flip angle (VFA) scan time. VFA scan time axis is in logarithmic scale. The top row represents brain tumor (BT) region of interest (ROI), and the bottom row represents the white matter (WM) ROI. The red dot represents the reference T_1 value in (A,B,E,F), and the undersampling level matching the prospective undersampling are marked bold in (C,D,G,H). As expected, precision gets monotonically worse with a higher undersampling factor. In the noiseless case, when $R \leq 16$ (VFA scan time $\geq$137.63 s), the T_1 bias is <1 ms and SD is <40 ms for both tissues. In the 3D-mimicking case, when $R \leq 10$, the T_1 bias is <10 ms and SD is <110 ms (WM) and <250 ms (BT)

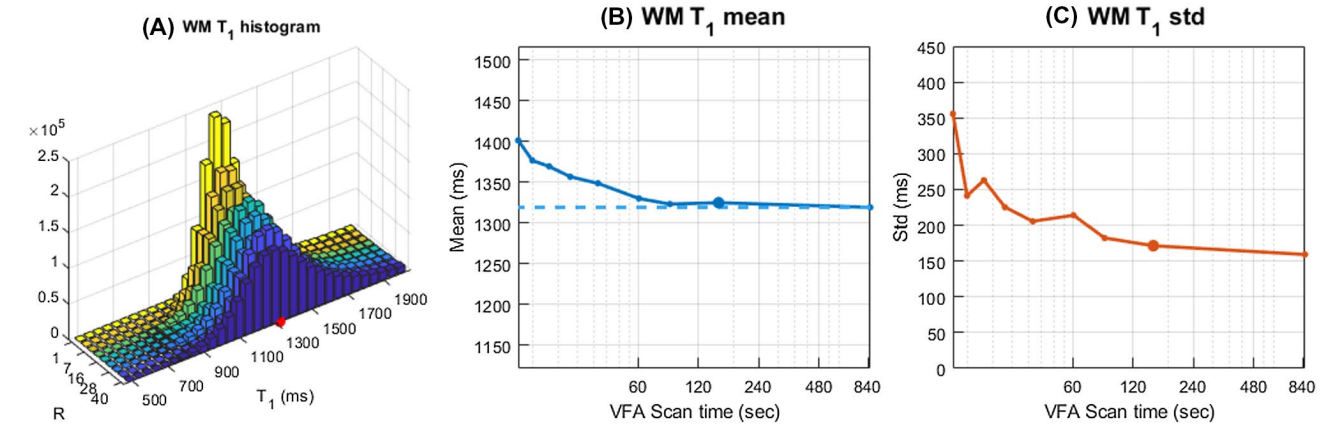

FIGURE 2 Healthy volunteer results. Fully sampled data sets were retrospectively undersampled with 10 realizations of the pseudorandom data sampling pattern. (A), White matter (WM) T_1 histogram as a function of undersampling factor. (B), Mean T_1. C, T_1 standard deviation (Std) as a function of variable flip angle (VFA) scan time. VFA scan time axis is in logarithmic scale. The mean T_1 from fully sampled data is shown as the blue dashed line in (B). Bias is insignificant (<30 ms) until $R \geq 16$. Precision gets worse with a higher undersampling factor, but imprecision caused by this method is not detectable until $R \geq 10$. When $R \leq 10$ (VFA scan time ≥100.8 s), T_1 mapping bias is <11 ms, and SD is <214 ms

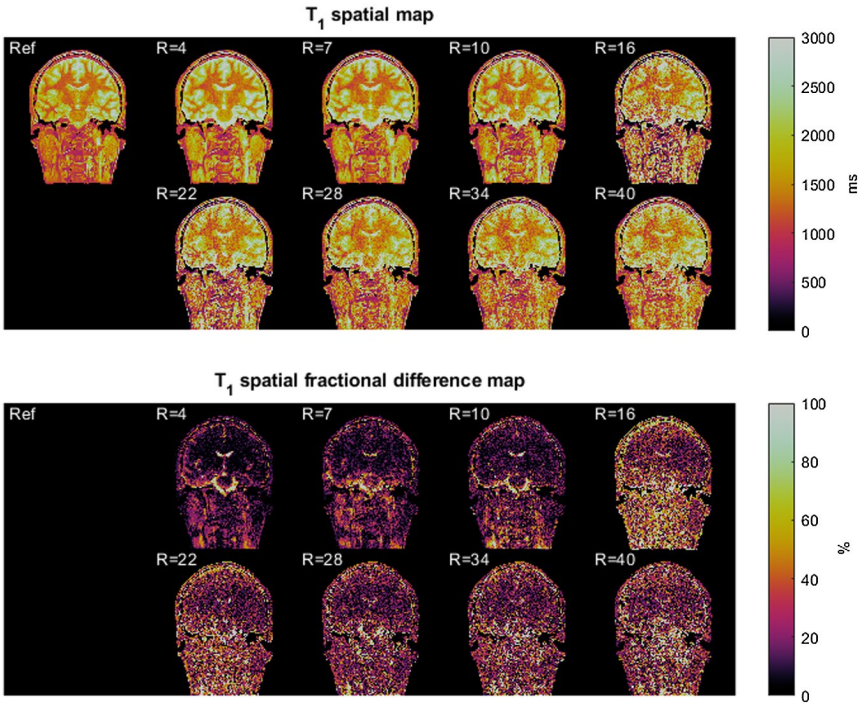

FIGURE 3 Illustration of T_1 spatial and absolute fractional difference maps from the healthy volunteer. Direct reconstruction of the fully sampled data is taken as the reference. Qualitatively, for $R \leq 10$, we see minor error in white matter (WM) or gray matter (GM). Errors appear isolated to cerebrospinal fluid (bias > 1278.5 ms, standard deviation [SD] > 557.6 ms) and muscle (bias > 156.9 ms, SD > 209.8 ms), whose T_1 values are generally less of interest in brain dynamic contrast-enhanced–magnetic resonance imaging. Importantly, no spatial patterns indicating systemic errors were observed in the error maps. For $R > 10$, we observed severe error corruption of T_1 maps in GM and WM regions

we observe in Figure 1. Bias is small until $R \geq 16$, and SD increases with higher undersampling factor, but imprecision caused by this method is not detectable until $R \geq 10$. When $R \leq 10$ (VFA scan time ≥100.8 s), Figure 2B, C show T_1 mapping bias <11 ms, and SD is <214 ms (COV <15%).

Figure 3 shows a series of T_1 spatial maps of a representative healthy volunteer for each undersampling factor, and the associated absolute fractional difference maps. When $R \leq 10$, there is less error within WM and GM in which mean fractional difference was <8.46% and <14.76%, respectively, and error concentrated around tissues of less interest. For example, bias in CSF and temporalis is, respectively, >1278.5 ms and >156.9 ms. No spatial patterns related to the data sampling method were observed. As R increases, we can observe error starting to increase in the WM and GM regions.

3.3 | Demonstration in patients with brain tumors

The prospective data set contained a variety of tumor locations and time points during treatment. Demographics,

TABLE 1 Patient demographics, qualitative scores, and T_1 values for white matter and brain tumor regions of interest

Sex	Age	Diagnostic score	WM T_1 (M ± SD) ms	BT T_1 (M ± SD) ms	Muscle T_1 (M ± SD) ms	Cavity T_1 (M ± SD) ms
F	59	2	895.0 ± 166.9	1763.2 ± 241.0	1517.8 ± 260.1	2564.3 ± 603.8
F	60	2	1003.5 ± 118.7	N/A	1683.8 ± 594.5	4621.4 ± 606.3
F	56	2	1000.4 ± 82.2	2314.3 ± 284.4	1636.0 ± 559.2	4638.4 ± 563.7
M	49	1	1094.2 ± 161.9	1856.7 ± 201.2	1444.6 ± 438.6	4541.8 ± 757.6
M	62	2	1086.4 ± 65.9	1981.6 ± 177.7	1582.9 ± 295.1	N/A
F	58	2	933.1 ± 79.9	1994.0 ± 257.7	1449.5 ± 255.0	N/A
F	71	2	1193.2 ± 92.3	N/A	1530.3 ± 256.7	4845.7 ± 506.9
M	80	2	1146.2 ± 65.2	1592.0 ± 128.7	1387.3 ± 429.7	N/A
M	42	2	1126.7 ± 142.0	N/A	1627.3 ± 374.1	5066.8 ± 865.7
F	71	2	1115.5 ± 84.2	1894.1 ± 227.4	1512.9 ± 364.1	3607.1 ± 530.5
F	61	2	1000.8 ± 51.3	1680.8 ± 155.2	1692.3 ± 356.2	4229.2 ± 265.6
F	67	2	1040.0 ± 66.2	1790.7 ± 99.0	1570.5 ± 152.0	2801.6 ± 180.7
F	52	2	1048.2 ± 92.8	1726.0 ± 177.5	1576.7 ± 397.3	N/A

Note: Volume T_1 data sets were qualitatively scored by a neuroradiologist using the following Likert scale: 0 = nondiagnostic; 1 = diagnostic with mediocre quality; 2 = diagnostic with high quality. Small ROIs were manually drawn to also yield T_1 measurements, reported as mean ± SD.

Abbreviations: BT, brain tumor; F, female; M, male; N/A, not applicable; ROIs, regions of interest; SD, standard deviation; WM, white matter.

qualitative diagnostic scores, and T_1 values of WM, BT, and temporalis and cavity-fillings are reported in Table 1. BT T_1 values are reported from the time point with the most clear and substantial evidence of tumor, determined based on the longitudinal progression verified by contrast enhancement. No distinct artifacts were observed. One case received a qualitative score of 1, and this case has strong T_1 inhomogeneity in CSF. All other cases received a qualitative score of 2. Out of 13 cases, three showed no obvious tumor based on T_1 and postcontrast readings, whereas all other cases showed brain tumor and/or postsurgical abnormalities. There is noticeably higher SD in temporalis T_1, and cavity-fillings have substantially longer T_1 (>4000 ms) than WM and BT. Figure 4 shows three representative examples with orthogonal cross sections of each tumor. These maps show clear T_1 differentiation of WM, GM, and BT abnormality regions, as well as postsurgical cavities, with high spatial resolution. Figure 5 shows zoomed versions of the same T_1 maps that showcase the ability to capture T_1 heterogeneity.

4 | DISCUSSION

This study evaluated the direct estimation of native M_0 and T_1 maps at 3T through simulation, as well as in in vivo studies of a healthy subject and patients with brain tumors. Simulations in DROs revealed T_1 measurement variability of this approach to be dominated by noise at undersampling factors ≤10, whereas errors caused by undersampling dominated above. We anticipate this cutoff point to differ for other field strengths (eg, 1.5T), coil configurations, protocols (eg, resolution, FOV), anatomies (eg, breast, prostate) and imaging tasks (eg, other quantitative MRI applications). Simulation on noise corrupted T_1 measurements also showed the T_1 errors in BT to be more susceptible to undersampling than in WM regions. Therefore, it is important to focus performance analysis on clinically relevant regions of interest rather than global metrics.

We used a 3D Fourier transform acquisition with Cartesian spiral subsampling because it is important to maintain the same spatial distortions between the T_1 mapping and the DCE sequence. These are largely impacted by the pulse sequence, prescription, and readout trajectory and bandwidth. A limitation of this study is that we did not compare different subsampling approaches. Such an analysis has been performed for sparse DCE-MRI acquisitions.[31] We used the same subsampling strategy for T_1 mapping as is being used for sparse DCE-MRI at our institution.

Results of retrospective in vivo scans were consistent with results from the 3T-mimicking noisy DRO, which confirms the ability of the simulation to predict in vivo performance. Specifically, both T_1 mean and SD values increased with higher undersampling, as shown in Figures 1C,D and 2B,C. Up to the critical undersampling factor of 10, the trend can be explained by noise amplification related to parallel imaging because the increase was only observed in the noisy cases. However, for undersampling factors above 10, the formulated problem becomes ill-posed, causing variations in the mean and increased SD in both noisy and noiseless cases. We

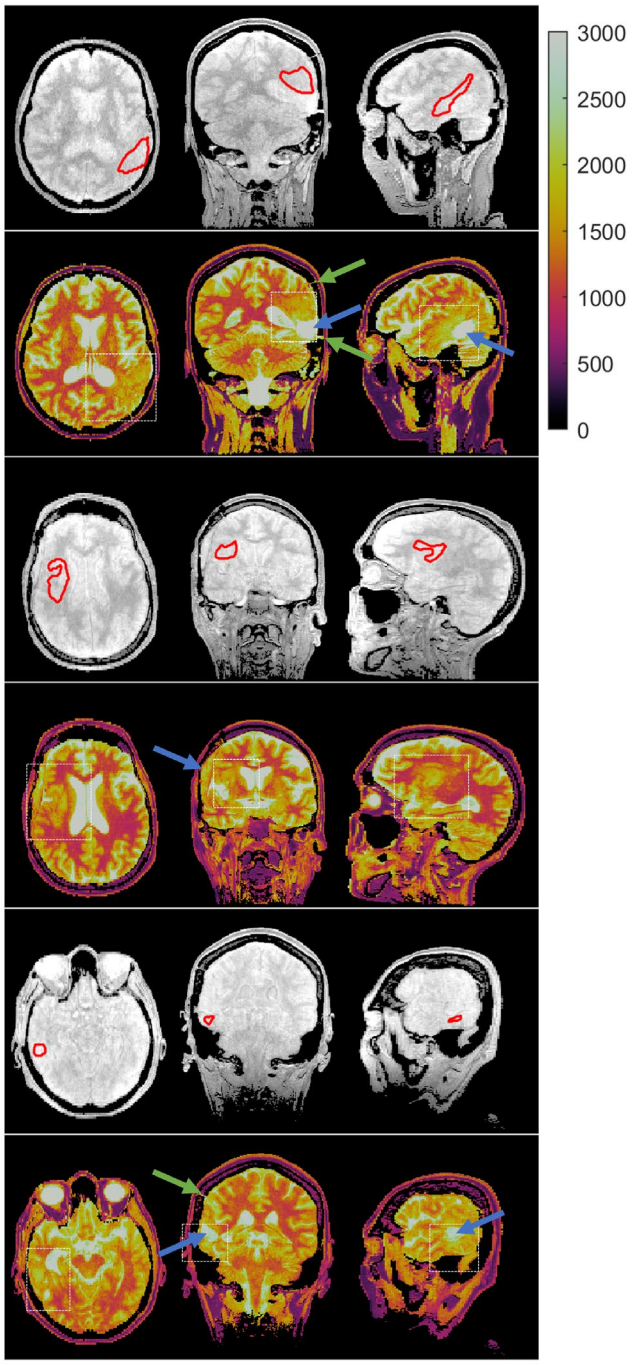

FIGURE 4 Representative M_0 and T_1 maps from three patients with high-grade glioma. Maps are volumetric, and axial, coronal, and sagittal slices through the tumor section for each patient (the first, the third, and the fifth row). M_0 maps with tumor region of interest drawn in red (the second, the fourth, and the sixth row). T_1 maps showing good delineation of white matter (WM), gray matter (GM), cerebrospinal fluid, and tumor. WM and GM regions have the expected homogeneity. In addition to tissue differential, these maps also reveal the locations of craniotomy (green arrow) and postsurgical cavities (blue arrow) that are filled with proteinaceous fluid such as blood in high spatial resolution

expect that this "critical R" is dependent on several factors, including the receiver coil configuration and the number of VFAs. For example, the critical R" is likely to be larger if one uses higher-density coil arrays that provide greater degrees of freedom in the subspace spanned by the coil sensitivity maps.

We noticed no spatial patterns related to data sampling in the T_1 error maps at $R \leq 10$ in the healthy volunteer study. There were, however, mild spatial variations in T_1 error with tissue type. For instance, we saw negligible error in WM and higher error in CSF. This is consistent with the expected reduction in T_1 precision as true T_1 increases. The proposed method was successfully applied to a small cohort of patients with high-grade glioma. The T_1 values in BT regions are heterogeneous and are longer than those of WM in the same subjects with values consistent with the literature[33-35] (1392-3601 ms).

We observed spatial heterogeneity and the presence of sharp features in BT ROI's. This indicates the need for precontrast T_1 mapping to provide equally fine spatial resolution compared with DCE-MRI and indicates that the use of spatial constraints/regularization could mask these features. Parametric constraints along the FA dimension or appropriately defined low-rank constraints may be viable. The proposed method allowed clear visualization of postsurgical cavities that have substantially longer T_1 values. The proposed method depicted the expected tissue boundaries with high spatial resolution and whole-brain coverage, providing adequate quality for voxel-wise quantitative DCE-MRI. However, we were not able to observe clear boundaries between cellular tumor and cavities, likely because there could be mixture with more complicated T_1 characteristics, such as edema.

Error propagation analysis revealed that ±15% error in mean brain-tumor T_1 results in at most 0.008 and 0.007 min^{-1} (Patlak model), and 0.016 and 0.033 min^{-1} absolute error extended Tofts-Kety (ETK) model in the DCE estimated pharmacokinetic parameters, v_p and K^t, respectively. However, there are many dependencies, and error propagation depends on the TK model, true T_1 and the polarity of the error. TK error is always positively related to precontrast T_1 error in the Patlak model; however, the relationships for the ETK model are more complicated as discussed in the Appendix A.

This study has several limitations. First, there is a general lack of commonly accepted glioma T_1 values likely because of intertumor heterogeneity because of factors such as tumor grade, age, and treatment. For this reason, realistic simulation of brain tumors in DROs remains challenging and possibly suboptimal in terms of its ability to accurately capture real-brain DCE-MRI examinations. This study addresses this with a range of parameter values based on the published literature, and refinement of this approach is subject to future research.

The second limitation consists of only using one healthy subject for in vivo validation of the proposed method. Acquiring fully sampled VFA scans is time consuming,

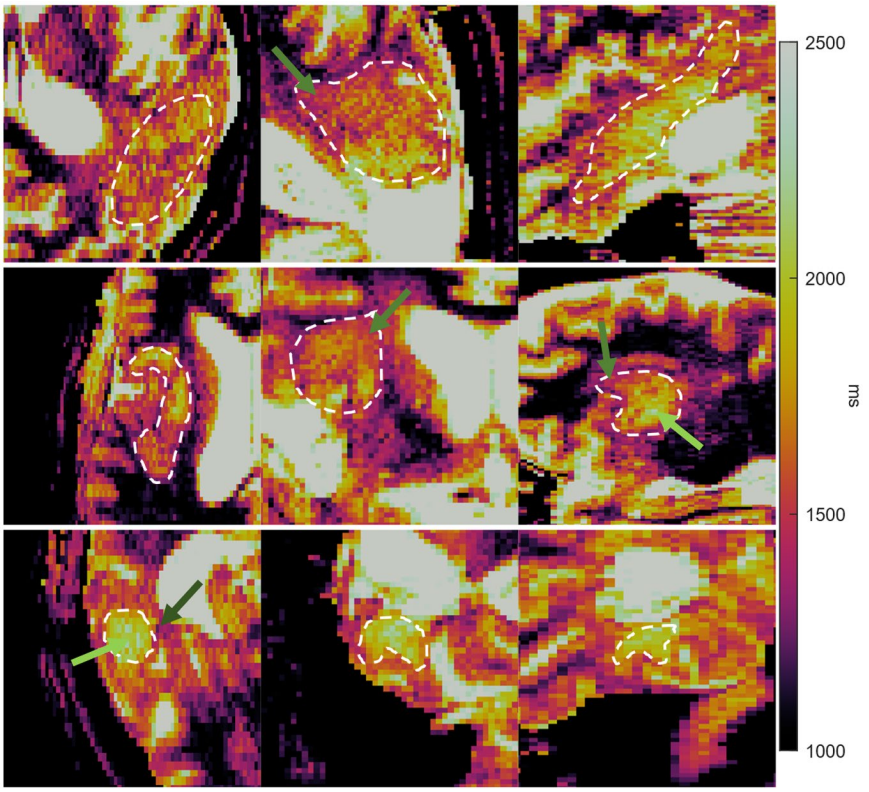

FIGURE 5 Closeup of T_1 maps from the three patients in Figure 4. Maps are zoomed into the tumor region (delineated by white dashed box in Figure 4), with narrow display range. The proposed method captures T_1 heterogeneity. T_1 coefficient of variation are 10.84%, 9.96%, and 7.31% for the top, middle, and bottom rows, respectively. All cases show spatial variations in T_1. For example, T_1 is longer in tumor center (eg, light green arrow) than in the tumor rim (eg, green arrow) and the peritumoral regions (eg, dark green arrow)

which impedes the generation of larger data sets for this study. For identical reasons, acquiring such scans for patients with brain tumors as the target cohort was not practical because of the severity of the disease and patient unwillingness to consent to such extensive research examinations. Tumor ROIs were directly drawn on the T_1 maps to be evaluated, which caused circularity in the patient study that we were unable to avoid.

Failure to account for magnetization transfer (MT) and motion effects is the third limitation of the study. Better accuracy and precision may be achieved by incorporating MT and head motion modeling, or by implementing controlled saturation MT introduced by Teixeira et al.[38] An example of showing improved MT-balanced VFA T_1 mapping has been shown by Lee et al.[39]

The fourth limitation is that the FA settings were not optimized for this application. We used seven FAs logarithmically spaced from 1° to 15° based on the expectation that T_1 values in BT ROIs can fall in a broad range. We used a large number of FAs to improve sensitivity over this broad range of T_1, but this was not optimized via simulation or phantom experiment.

Finally, the proposed reconstruction involves a nonlinear and nonconvex optimization problem. This is computationally complex and can be numerically unstable. In the prospective study, reconstruction required roughly 3 h per 3D data set, on a computation node of the USC Center for Advanced Research Computing. The long reconstruction time is caused by the recurring gradient computation. This can be potentially shortened with better initial guesses such as low-resolution estimates of M_0 and T_1 maps.

In this study, 10-fold undersampling was found to be the upper bound for adequately accurate precontrast T_1 mapping. This result is specific to the body part and disease of interest, and our DCE-MRI setup, including field strength, receiver coil, and imaging parameters. To apply this approach to a different scanner or body part and disease, we suggest starting with a disease-appropriate DRO, locally measured coil-sensitivity profiles, and noise-covariance measurements. Then repeat the steps in this article to determine the undersampling limit. We have provided software to facilitate this process (see Data Availability Statement).

5 | CONCLUSION

We have shown the feasibility of direct precontrast T_1 mapping suitable for high-resolution whole-brain quantitative DCE-MRI, with 150 s of VFA scan time. The proposed method is validated in DROs and in one healthy volunteer, and achieved T_1 bias $\leq$ 11 ms and COV $\leq$ 15% at an undersampling factor of 4. Prospective application to BT patients showed no distinct artifacts, diagnostic image quality, and T_1 maps with high definition and with values consistent with the published literature.

ACKNOWLEDGMENTS

The authors thank Sreedevi Gutta, Nam Gyun Lee, and Ye Tian for helpful discussions. The authors gratefully acknowledge funding from the National Institutes of Health (Grant No. R33-CA225400, principal investigator: Krishna S. Nayak) and the Canadian Cancer Society Research Institute (for patient scanning).

CONFLICT OF INTEREST

Coauthor R. Marc Lebel is an employee of GE Healthcare. The authors declare that they have no competing interests.

DATA AVAILABILITY STATEMENT

The source code for the Sparse Pre-Contrast T_1 Mapping for High-Resolution Whole-Brain DCE-MRI is available at https://github.com/usc-mrel/SparsePreT1_DCE. The noiseless and 3T-mimicking noisy brain tumor DRO, the tumor ROI data, and the Cartesian spiral sampling pattern generator used in this work are provided within the same package.

ORCID

Zhibo Zhu https://orcid.org/0000-0002-2130-1158
Yannick Bliesener https://orcid.org/0000-0001-5436-1918
Krishna S. Nayak https://orcid.org/0000-0001-5735-3550

REFERENCES

1. Tofts PS, Brix G, Buckley DL, et al. Estimating kinetic parameters from dynamic contrast-enhanced t1-weighted MRI of a diffusable tracer: standardized quantities and symbols. *J Magn Reson Imaging*. 1999;10:223-232.
2. Sourbron SP, Buckley DL. On the scope and interpretation of the Tofts models for DCE-MRI. *Magn Reson Med*. 2011;66:735-745.
3. O'Connor JPB, Jackson A, Parker GJM, Roberts C, Jayson GC. Dynamic contrast-enhanced MRI in clinical trials of antivascular therapies. *Nat Rev Clin Oncol*. 2012;9:167-177.
4. Heye AK, Culling RD, Valdés Hernández MDC, Thrippleton MJ, Wardlaw JM. Assessment of blood-brain barrier disruption using dynamic contrast-enhanced MRI. A systematic review. *NeuroImage Clin*. 2014;6:262-274.
5. Law M, Yang S, Babb JS, et al. Comparison of cerebral blood volume and vascular permeability from dynamic susceptibility contrast-enhanced perfusion MR imaging with glioma grade. *Am J Neuroradiol*. 2004;25:746-755.
6. Larsson HBW, Stubgaard M, Frederiksen JL, Jensen M, Henriksen O, Paulson OB. Quantitation of blood-brain barrier defect by magnetic resonance imaging and gadolinium-DTPA in patients with multiple sclerosis and brain tumors. *Magn Reson Med*. 1990;16:117-131.
7. Cramer SP, Simonsen H, Frederiksen JL, Rostrup E, Larsson HBW. Abnormal blood-brain barrier permeability in normal appearing white matter in multiple sclerosis investigated by MRI. *NeuroImage Clin*. 2014;4:182-189.
8. Yang S, Law M, Zagzag D, et al. Dynamic contrast-enhanced perfusion MR imaging measurements of endothelial permeability: differentiation between atypical and typical meningiomas. *AJNR Am J Neuroradiol*. 2003;24:1554-1559.
9. Montagne A, Barnes S, Sweeney M, et al. Blood-Brain barrier breakdown in the aging human hippocampus. *Neuron*. 2015;85:296-302.
10. Pruessmann KP, Weiger M, Scheidegger MB, Boesiger P. SENSE: sensitivity encoding for fast MRI. *Magn Reson Med*. 1999;42:952-962.
11. Uecker M, Lai P, Murphy MJ, et al. ESPIRiT—an eigenvalue approach to autocalibrating parallel MRI: where SENSE meets GRAPPA. *Magn Reson Med*. 2014;71:990-1001.
12. Lustig M, Donoho D, Pauly JM. Sparse MRI: the application of compressed sensing for rapid MR imaging. *Magn Reson Med*. 2007;58:1182-1195.
13. Lebel RM, Jones J, Ferre J-C, Law M, Nayak KS. Highly accelerated dynamic contrast enhanced imaging. *Magn Reson Med*. 2014;71:635-644.
14. Guo YI, Lebel RM, Zhu Y, et al. High-resolution whole-brain DCE-MRI using constrained reconstruction: prospective clinical evaluation in brain tumor patients. *Med Phys*. 2016;43:2013-2023.
15. Dickie BR, Banerji A, Kershaw LE, et al. Improved accuracy and precision of tracer kinetic parameters by joint fitting to variable flip angle and dynamic contrast enhanced MRI data. *Magn Reson Med*. 2016;76:1270-1281.
16. Guo Y, Lingala SG, Zhu Y, Lebel RM, Nayak KS. Direct estimation of tracer-kinetic parameter maps from highly undersampled brain dynamic contrast enhanced MRI. *Magn Reson Med*. 2017;78:1566-1578.
17. Guo Y, Lingala SG, Bliesener Y, Lebel RM, Zhu Y, Nayak KS. Joint arterial input function and tracer kinetic parameter estimation from undersampled dynamic contrast-enhanced MRI using a model consistency constraint. *Magn Reson Med*. 2018;79:2804-2815.
18. Lingala SG, Guo YI, Bliesener Y, et al. Tracer kinetic models as temporal constraints during brain tumor DCE-MRI reconstruction. *Med Phys*. 2020;47:37-51.
19. Fram EK, Herfkens RJ, Johnson GAllan, et al. Rapid calculation of T1 using variable flip angle gradient refocused imaging. *Magn Reson Imaging*. 1987;5:201-208.
20. Look DC, Locker DR. Time saving in measurement of NMR and EPR relaxation times. *Rev Sci Instrum*. 1970;41:250-251.
21. Lebel RM, Guo Y, Lingala SG, Frayne R, Nayak KS. Highly accelerated DCE imaging with integrated T1 mapping. In: *ISMRM 25th Scientific Sessions*. Honolulu; 2017, p. 138.
22. Maier O, Schoormans J, Schloegl M, et al. Rapid T 1 quantification from high resolution 3D data with model-based reconstruction. *Magn Reson Med*. 2019;81:2072-2089.
23. Deoni SCL. High-resolution T1 mapping of the brain at 3T with driven equilibrium single pulse observation of T1 with high-speed incorporation of RF field inhomogeneities (DESPOT1-HIFI). *J Magn Reson Imaging*. 2007;26:1106-1111.
24. Deoni SCL, Rutt BK, Peters TM. Rapid combined T1 and T2 mapping using gradient recalled acquisition in the steady state. *Magn Reson Med*. 2003;49:515-526.
25. Larsson C, Kleppestø M, Grothe I, Vardal J, Bjørnerud A. T_1 in high-grade glioma and the influence of different measurement strategies on parameter estimations in DCE-MRI. *J Magn Reson Imaging*. 2015;42:97-104.

26. Fennessy FM, Fedorov A, Gupta SN, Schmidt EJ, Tempany CM, Mulkern RV. Practical considerations in T1 mapping of prostate for dynamic contrast enhancement pharmacokinetic analyses. *Magn Reson Imaging*. 2012;30:1224-1233.
27. Sutton BP, Noll DC, Fessler JA. Fast, iterative image reconstruction for MRI in the presence of field inhomogeneities. *IEEE Trans Med Imaging*. 2003;22:178-188.
28. Cheng H-LM, Wright GA. Rapid high-resolutionT1 mapping by variable flip angles: accurate and precise measurements in the presence of radiofrequency field inhomogeneity. *Magn Reson Med*. 2006;55:566-574.
29. Lee Y, Callaghan MF, Nagy Z. Analysis of the precision of variable flip angle T1 mapping with emphasis on the noise propagated from RF transmit field maps. *Front Neurosci*. 2017;11:106.
30. Bosca RJ, Jackson EF. Creating an anthropomorphic digital MR phantom—an extensible tool for comparing and evaluating quantitative imaging algorithms. *Phys Med Biol*. 2016;61:974-982.
31. Bliesener Y, Lingala SG, Haldar JP, Nayak KS. Impact of (k, t) sampling on DCE MRI tracer kinetic parameter estimation in digital reference objects. *Magn Reson Med*. 2020;83:1625-1639.
32. Stanisz GJ, Odrobina EE, Pun J, et al. T1, T2 relaxation and magnetization transfer in tissue at 3T. *Magn Reson Med*. 2005;54:507-512.
33. Müller A, Jurcoane A, Kebir S, et al. Quantitative T1-mapping detects cloudy-enhancing tumor compartments predicting outcome of patients with glioblastoma. *Cancer Med*. 2017;6:89-99.
34. Hattingen E, Müller A, Jurcoane A, et al. Value of quantitative magnetic resonance imaging T1-relaxometry in predicting contrast-enhancement in glioblastoma patients. *Oncotarget*. 2017;8:53542-53551.
35. Badve C, Yu A, Dastmalchian S, et al. MR fingerprinting of adult brain tumors: initial experience. *Am J Neuroradiol*. 2017;38:492-499.
36. Sacolick LI, Wiesinger F, Hancu I, Vogel MW. B 1 mapping by Bloch-Siegert shift. *Magn Reson Med*. 2010;63:1315-1322.
37. Zhang Y, Brady M, Smith S. Segmentation of brain MR images through a hidden Markov random field model and the expectation-maximization algorithm. *IEEE Trans Med Imaging*. 2001;20:45-57.
38. A.G. Teixeira RP, Malik SJ, Hajnal JV. Fast quantitative MRI using controlled saturation magnetization transfer. *Magn Reson Med*. 2019;81:907-920.
39. Lee N, Zhu Z, Nayak KS. Variable flip angle T1 mapping with MT-balanced RF pulses. In: *Proceedings of the ISMRM & SMRT Virtual Conference & Exhibition*, 2020, p. 3793.
40. Parker GJM, Roberts C, Macdonald A, et al. Experimentally-derived functional form for a population-averaged high-temporal-resolution arterial input function for dynamic contrast-enhanced MRI. *Magn Reson Med*. 2006;56:993-1000.
41. Georgiou L, Wilson DJ, Sharma N, Perren TJ, Buckley DL. A functional form for a representative individual arterial input function measured from a population using high temporal resolution DCE MRI. *Magn Reson Med*. 2019;81:1955-1963.

SUPPORTING INFORMATION

Additional Supporting Information may be found online in the Supporting Information section.

FIGURE S1 Illustration of Cartesian spiral sampling. Each panel illustrates the (k_y, k_z) matrix with white dots denoting the phase encodes that are acquired. Flip angles are logarithmically spaced from 1.5° to 15°. An undersampling factor R = 10 is illustrated, which corresponds to 60.48 seconds VFA scan time. Note that 15° is 4 times more densely sampled than other FA's, for all undersampling factors

How to cite this article: Zhu Z, Lebel RM, Bliesener Y, Acharya J, Frayne R, Nayak KS. Sparse precontrast T_1 mapping for high-resolution whole-brain DCE-MRI. *Magn Reson Med*. 2021;86:2234–2249. https://doi.org/10.1002/mrm.28849

APPENDIX A

IMPACT OF PRECONTRAST T_1 (ERRORS) ON QUANTITATIVE DCE-MRI (ERRORS)

Here, we summarize the impact of precontrast T_1 mapping errors on quantitative dynamic contrast-enhanced–magnetic resonance imaging (DCE-MRI) tracer-kinetic (TK) parameter mapping errors. This is a form of error propagation analysis. DCE-MRI TK parameters θ, can include K^t, v_p, v_e, etc., depending on the model used. Here, we examine the Patlak and extended Tofts-Kety (ETK) models, which are commonly used in brain tumor DCE-MRI.

DCE-MRI uses spoiled gradient echo (SPGR) imaging. Consider the steady-state SPGR signal equation:

$$D_t\left(M_0, T_1, C(t), \alpha\right) = M_0 \frac{\left(1 - E_1(t)\right)\sin\alpha}{1 - E_1(t)\cos\alpha} \tag{A1}$$

where M_0 is the equilibrium magnetization, T_1 is the precontrast longitudinal relaxation time, $C(t)$ is the contrast agent concentration, α is the flip angle (FA), and $E_1(t) = E_{10}e^{-TR\cdot r_1 C(t)}$ with $E_{10} = e^{-TR\cdot R_1}$ and $R_1 = 1/T_1$, according to the fast exchange limit (FXL). We can estimate the first-order error by:

$$\Delta\theta = \frac{\partial\theta}{\partial T_1}\Delta T_1 \tag{A2}$$

Therefore, we must evaluate one partial derivative, which is possible using the chain rule:

$$\frac{\partial\theta}{\partial T_1} = \sum_{i=1}^{N} \frac{\partial\theta}{\partial C\left(t_i\right)} \frac{\partial C\left(t_i\right)}{\partial R_1} \frac{\partial R_1}{\partial T_1} \tag{A3}$$

where θ is the TK parameter of interest, for example, v_p or K^t. We are evaluating the dependence on the estimated T_1 (and not the DCE scan or vascular input function estimation). Therefore,

we compute the partial derivative of estimated concentration ($C(t_i)$) as a function of precontrast T_1, given measured DCE signals as constants. We differentiate both sides of Equation (A1) with respect to (w.r.t.) to get:

$$\begin{aligned} 0 &= M_0 \frac{\sin\alpha \cdot TR \cdot E_1(t)}{\left(1 - E_1(t)\cos\alpha\right)^2} (1-\cos\alpha) \cdot \frac{\partial \left[R_1 + r_1 C(t_i)\right]}{\partial R_1} \\ &= M_0 \frac{\sin\alpha \cdot TR \cdot E_1(t)}{\left(1 - E_1(t)\cos\alpha\right)^2} (1-\cos\alpha) \left[1 + r_1 \frac{\partial C(t_i)}{\partial R_1}\right] \end{aligned} \tag{A4}$$

Therefore, we have:

$$\frac{\partial C(t_i)}{\partial R_1} = -\frac{1}{r_1} \tag{A5}$$

This is the same for all time points. As a result, we have:

$$\frac{\partial \theta}{\partial T_1} = \frac{1}{r_1 T_1^2} \sum_{i=1}^{N} \frac{\partial \theta}{\partial C(t_i)} \tag{A6}$$

Patlak model

Consider first the Patlak model, which is a widely used linear compartment model. According to the Patlak model CA concentration is a linear function of the tracer-kinetic parameters:

$$C(t) = C_p(t)\, v_p + K^t \int_0^t C_p(\tau)\, d\tau \tag{A7}$$

where $C_p(t)$ is the time-varying contrast agent plasma volume concentration (mM). $C_p(t)$ is often called the vascular input function (VIF). The function should be determined by sampling the delivery of contrast agent from a vessel directly interacting with the tissue of interest. In this Appendix, three $C_p(t)$s were either generated from different population-based models (Parker et al[40] and Georgiou et al[41]) or estimated by averaging multiple in vivo data from our patient DCE-MRI study. This model can be expressed as a matrix-vector multiplication, as follows:

$$\mathbf{C}_t = \begin{bmatrix} C(t_1) \\ C(t_2) \\ \vdots \\ C(t_N) \end{bmatrix} = \mathbf{A} \begin{bmatrix} v_p \\ K^t \end{bmatrix} \tag{A8}$$

$$\mathbf{A} = \begin{bmatrix} C_p(t_1) \int_0^{t_1} C_p(\tau)\, d\tau \\ C_p(t_2) \int_0^{t_2} C_p(\tau)\, d\tau \\ \vdots \qquad\qquad \vdots \\ C_p(t_N) \int_0^{t_N} C_p(\tau)\, d\tau \end{bmatrix} \tag{A9}$$

The solution for $\begin{bmatrix} v_p \\ K^t \end{bmatrix}$ that minimizes the sum of squared residuals (also called the least-squares solution) is:

$$\begin{bmatrix} v_p \\ K^t \end{bmatrix} = \mathbf{A}^{\dagger} \mathbf{C}_t \tag{A10}$$

v_p and K^t are linear functions of $\mathbf{C}_t$; therefore, all partial derivatives for the least-squares estimator reside as entries in the $\mathbf{A}^{\dagger}$ matrix as follows:

$$\begin{bmatrix} \frac{\partial v_p}{\partial \mathbf{C}_t} \\ \frac{\partial K^t}{\partial \mathbf{C}_t} \end{bmatrix} = \begin{bmatrix} \frac{\partial v_p}{\partial C(t_1)} & \frac{\partial v_p}{\partial C(t_2)} \cdots \frac{\partial v_p}{\partial C(t_N)} \\ \frac{\partial K^t}{\partial C(t_1)} & \frac{\partial K^t}{\partial C(t_2)} \cdots \frac{\partial K^t}{\partial C(t_N)} \end{bmatrix} = \mathbf{A}^{\dagger} \tag{A11}$$

Extended Tofts-Kety model

As another model widely used in the evaluation of brain tumors, consider the extended Tofts-Kety (ETK) model, which has a nonlinear dependence on vascular parameters. The ETK model is as follows:

$$C(t) = C_p(t)\, v_p + K^t \int_0^t C_p(\tau)\, e^{-k_{ep}(t-\tau)} d\tau \tag{A12}$$

where $k_{ep} = \frac{K^t}{v_e}$ is a rate constant.

Although the model nonlinearity does not allow for an explicit solution to the vascular parameter estimator, local first derivatives can be obtained through implicit differentiation or an additional linearization step. In the following, we assume constant v_e constant for simplicity.

We take the derivative w.r.t. $C(t_i)$ on both sides of Equation (12) to get:

$$\begin{aligned} 1 = {} & C_p(t_i) \frac{\partial v_p}{\partial C(t_i)} + \frac{\partial K^t}{\partial C(t_i)} \int_0^{t_i} C_p(\tau)\, e^{-k_{ep}(t_i-\tau)} d\tau \\ & + \frac{\partial K^t}{\partial C(t_i)} K^t \int_0^{t_i} -\frac{t_i - \tau}{v_e} C_p(\tau)\, e^{-k_{ep}(t_i-\tau)} d\tau \end{aligned} \tag{A13}$$

This will convert the nonlinear model of parameters to a linear model of partial derivatives. Thus, we can construct another matrix-vector multiplication as follows:

$$1_i = \mathbf{A} \begin{bmatrix} \frac{\partial v_p}{\partial C(t_i)} \\ \frac{\partial K^t}{\partial C(t_i)} \end{bmatrix} \tag{A14}$$

In which 1_i is a column vector whose ith entry is 1, and

$$\mathbf{A}=\begin{bmatrix} C_p\left(t_1\right)\int_0^{t_1}\left(1-K^t\frac{t_1-\tau}{v_e}\right)C_p\left(\tau\right)e^{-k_{ep}\left(t_1-\tau\right)}d\tau \\ C_p\left(t_2\right)\int_0^{t_2}\left(1-K^t\frac{t_2-\tau}{v_e}\right)C_p\left(\tau\right)e^{-k_{ep}\left(t_2-\tau\right)}d\tau \\ \vdots \\ C_p\left(t_N\right)\int_0^{t_N}\left(1-K^t\frac{t_N-\tau}{v_e}\right)C_p\left(\tau\right)e^{-k_{ep}\left(t_N-\tau\right)}d\tau \end{bmatrix} \quad \text{(A15)}$$

When $\mathbf{A}$ is evaluated at some $K^t=k$, the derivatives are the least-squares solution to Equation (A14), that is,

$$\left.\begin{bmatrix}\frac{\partial v_p}{\partial C\left(t_i\right)} \\ \frac{\partial K^t}{\partial C\left(t_i\right)}\end{bmatrix}\right|_{K^t=k}=\mathbf{A}^{\dagger}1_i \quad \text{(A16)}$$

Alternatively, we can use linear approximation. A continuous and differentiable function $f(\boldsymbol{x})$ can be well approximated around $\boldsymbol{x}=\tilde{\boldsymbol{x}}$ by

$$f(\boldsymbol{x})\approx\left.\frac{df(x)}{d\boldsymbol{x}}\right|_{x=\tilde{x}}\boldsymbol{x}+\left[f(\%\tilde{\boldsymbol{x}})-\left.\frac{df(x)}{d\boldsymbol{x}}\right|_{x=\tilde{x}}\tilde{\boldsymbol{x}}\right] \quad \text{(A17)}$$

Equation (A12) can be linearly approximated at some $K^t=k$ as follows:

$$C\left(t_i\right)=C_p\left(t_i\right)v_p+\left.\frac{\partial C\left(t_i\right)}{\partial K^t}\right|_{K^t=k}K^t+r\left(k,t_i\right) \quad \text{(A18)}$$

In which

$$\left.\frac{\partial C\left(t_i\right)}{\partial K^t}\right|_{K^t=k}=\int_0^{t_i}\left(1-k\frac{t_i-\tau}{v_e}\right)C_p\left(\tau\right)e^{-\frac{k}{v_e}\left(t_i-\tau\right)}d\tau \quad \text{(A19)}$$

$$r\left(k,t_i\right)=k\int_0^{t_i}C_p\left(\tau\right)e^{-\frac{k}{v_e}\left(t_i-\tau\right)}d\tau-\left.\frac{\partial C\left(t_i\right)}{\partial K^t}\right|_{K^t=k}k \quad \text{(A20)}$$

We then can construct another matrix-vector multiplication such as

$$\mathbf{C}_t-\boldsymbol{r}\left(k,\boldsymbol{t}\right)=\mathbf{A}\begin{bmatrix}v_p\\K^t\end{bmatrix} \quad \text{(A21)}$$

In which

$$\mathbf{A}=\begin{bmatrix} C_p\left(t_1\right)\left.\frac{\partial C\left(t_1\right)}{\partial K^t}\right|_{K^t=k} \\ C_p\left(t_2\right)\left.\frac{\partial C\left(t_2\right)}{\partial K^t}\right|_{K^t=k} \\ \vdots \\ C_p\left(t_N\right)\left.\frac{\partial C\left(t_N\right)}{\partial K^t}\right|_{K^t=k} \end{bmatrix} \quad \text{(A22)}$$

Like Equation (A10), the least-squares solution to Equation (A21) is

$$\begin{bmatrix}v_p\\K^t\end{bmatrix}\approx\mathbf{A}^{\dagger}\left[\mathbf{C}_t-\boldsymbol{r}\left(k,\boldsymbol{t}\right)\right] \quad \text{(A23)}$$

Similar to Equation (A11), the derivatives reside as follows:

$$\left.\begin{bmatrix}\frac{\partial v_p}{\partial C\left(t_i\right)} \\ \frac{\partial K^t}{\partial C\left(t_i\right)}\end{bmatrix}\right|_{K^t=k}=\begin{bmatrix}\frac{\partial v_p}{\partial C\left(t_1\right)} & \frac{\partial v_p}{\partial C\left(t_2\right)} & \cdots & \frac{\partial v_p}{\partial C\left(t_N\right)} \\ \frac{\partial K^t}{\partial C\left(t_1\right)} & \frac{\partial K^t}{\partial C\left(t_2\right)} & \cdots & \frac{\partial K^t}{\partial C\left(t_N\right)}\end{bmatrix}=\mathbf{A}^{\dagger} \quad \text{(A24)}$$

Error propagation analysis

Error propagation analysis was performed for the two TK models as outlined in the previous section. The analysis was evaluated with three different VIFs and three different k_{ep} values (if necessary) to show the dependencies on them. In addition, all analysis assumed a T_1 range of 1700 ± 255 ms, roughly matching the mean T_1 of brain tumor in our patient study with ±15% variations.

Figure A1 shows error propagation analysis results in the Patlak model. The first row shows partial derivatives of v_p and K^t of precontrast T_1 values (1700 ± 255 ms). The second row shows the first-order error of v_p and K^t as a function of ±255 ms (±15%) ΔT_1 for the VIFs by Parker et al[40] (blue), Georgiou et al[41] (red), and the cohort-based in vivo brain VIF measured at our institution. As the first row shows, partial derivatives were positive and decreased as T_1 increased. Consequently, errors in TK parameters were positively related to T_1 errors, and T_1 error propagation was slower as T_1 increased. Quantitatively, a ±255 ms ΔT_1 results in ±0.0064, ±0.0043, and ±0.0085 error in v_p, and ±0.0074 min^{-1}, ±0.0053 min^{-1}, and ±0.0028 min^{-1} error in K^t in Parker's, Georgiou's, and in vivo measured VIF, respectively.

Figure A2 shows the partial derivatives of v_p and K^t of precontrast T_1 values (1700 ± 255 ms) in the ETK model. The first row shows the two-dimensional (2D) plot of partial derivatives of v_p. The second row shows the 2D plot of partial derivatives of K^t as a function of both rate constant k_{ep} and T_1. Like the Patlak model, both derivatives monotonically decreased as T_1 increases; however, they are not monotonic functions of k_{ep}. Especially for the partial derivative of K^t, it reached its positive extreme at k_{ep} approximately 0.64, 0.62, and 0.54 min^{-1}, and had polarity change at k_{ep} approximately 1.35, 1.32, and 0.92 min^{-1}.

Figure A3 shows the first-order error in v_p and K^t as a function of ΔT_1 in the ETK model in the first and second row, respectively. Errors are plotted for ±255 ms (±15%) ΔT_1 for Parker et al's[40] (left), Georgiou et al's[41] (middle), and in vivo measured (right) VIFs. Errors were also evaluated at three

different k_{ep} values to show dependencies on k_{ep}. Δv_p was positively related to ΔT_1; however, it shrank and then was amplified at k_{ep} increases. With ±255 ms ΔT_1, Δv_p extended to ±0.015, ±0.010, and ±0.016 in maximum at $k_{ep} = 1.5$ min^{-1} for Parker et al's, Georgiou et al's, and in vivo measured VIF, respectively. For ΔK^t, the result is more complicated because of the derivative polarity change. With ±255 ms ΔT_1, ΔK^t extended to ±0.008, ±0.007, and ±0.020 in maximum at $k_{ep} = 1.5$ min^{-1} for Parker et al's, Georgiou et al's, and in vivo measured VIF, respectively. Note that $k_{ep} = 1.5$ min^{-1} did not necessarily give the maximum ΔK^t; however, it was of more interest because high k_{ep} values were expected in tumor regions.

Briefly, an error of ±15% in mean brain tumor T_1 results in at most 0.008 and 0.007 min^{-1} absolute error (Patlak model), and 0.016 and 0.033 min^{-1} absolute error (ETK model) in the DCE-estimated pharmacokinetic parameters, v_p and K^t, respectively.

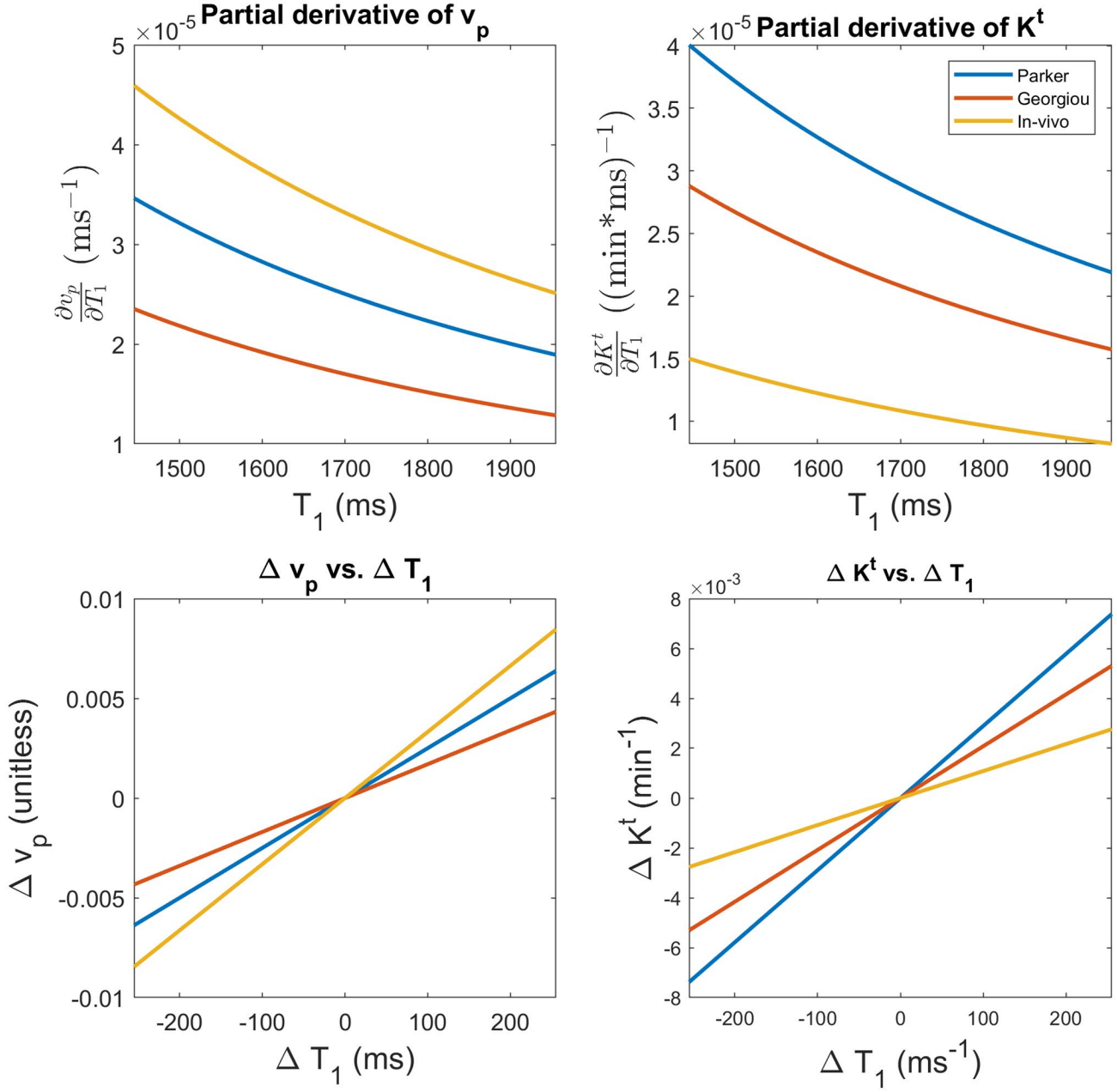

FIGURE A1 Error analysis in tracer-kinetic (TK) estimation in the Patlak model. The first row shows partial derivatives of v_p and K^t of precontrast T_1 values (1700 ± 255 ms). The second row shows the first-order error of v_p and K^t as a function of ±255 ms (±15%) ΔT_1. Parker's (blue), Georgiou's (red), and in vivo measured (yellow) vascular input functions (VIFs) were analyzed. As the first row shows, partial derivatives were positive and decreased as T_1 increased. Consequently, errors in TK parameters were positively related to T_1 errors, and T_1 error propagation was slower when T_1 increased. As the second row shows, a ±255 ms (±15%) ΔT_1 results in ±0.0064, ±0.0043, and ±0.0085 errors in v_p, and ±0.0074 min^{-1}, ±0.0053 min^{-1}, and ±0.0028 min^{-1} errors in K^t in Parker's, Georgiou's and in vivo measured VIF, respectively

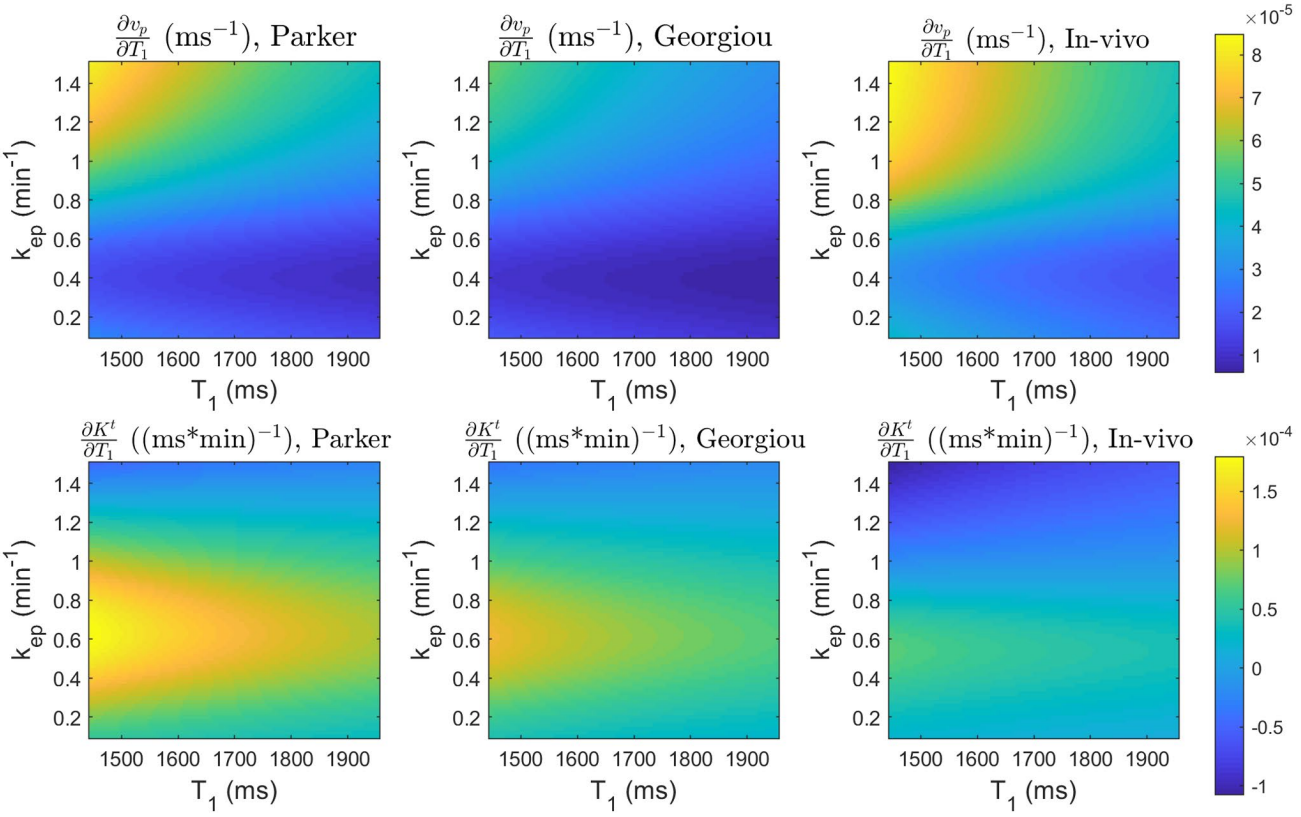

FIGURE A2 Partial derivatives of v_p and K^t of precontrast T_1 values (1700 ± 255 ms) in the ETK model. The 1st row shows the 2D plot of partial derivatives of v_p, and the 2nd row shows the 2D plot of partial derivatives of K^t as a function of both rate constant k_{ep} and T_1. Like the Patlak model, both derivatives monotonically decreased as T_1 increases, however, they are not monotonic functions of k_{ep}. Especially for the partial derivative of K^t, it had different polarities depending on k_{ep} value

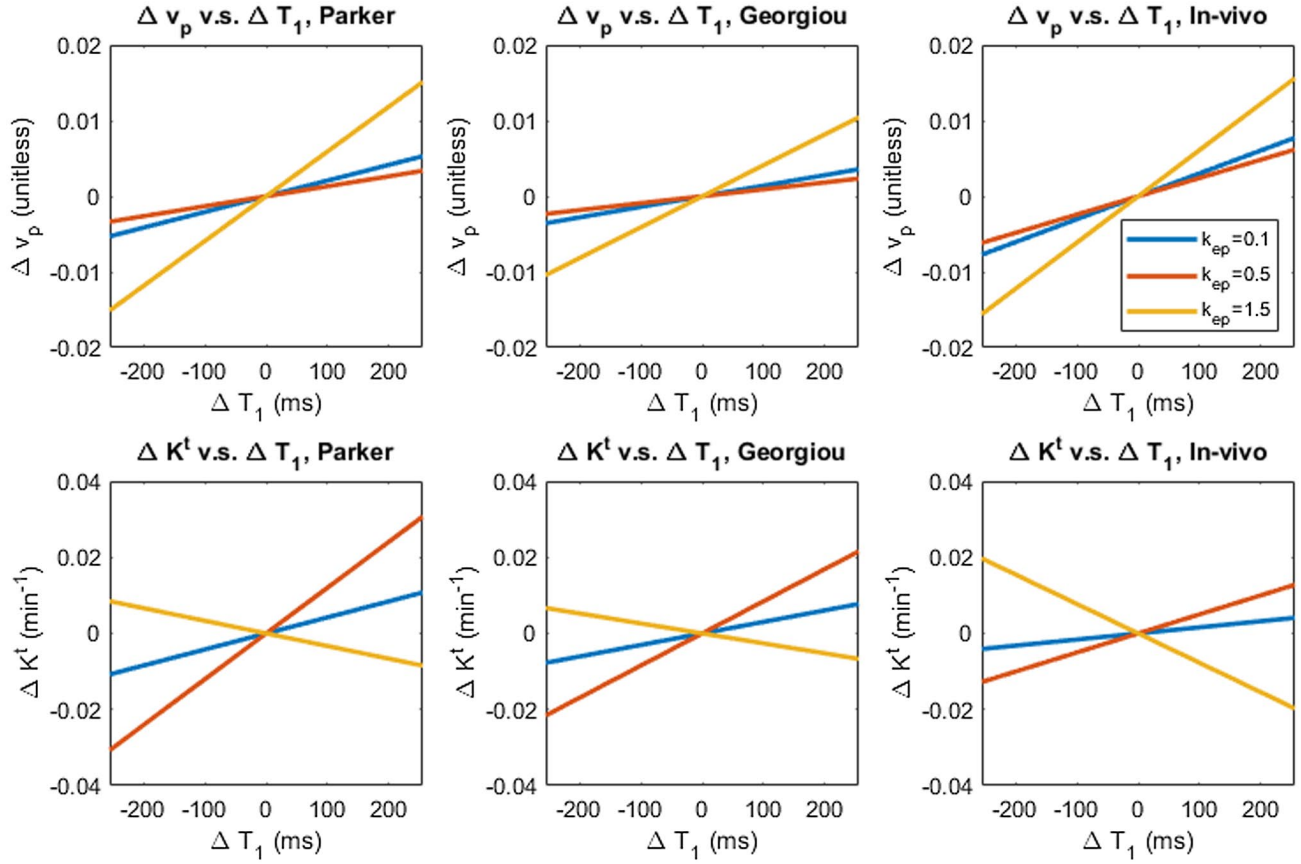

FIGURE A3 The first-order error in tracer-kinetic (TK) parameters as a function of ΔT_1 in the extended Tofts-Kety (ETK) model. Errors are plotted for ±255 ms (±15%) ΔT_1. The first and second row show the first-order error of v_p and K^t, respectively, and errors were analyzed using Parker's (left), Georgiou's (middle), and in vivo measured (right) vascular input function. Errors were also evaluated at three different k_{ep} values to show dependencies on k_{ep}. For v_p, the result is similar to that in Patlak model, whereas it is noticeable that Δv_p will be amplified at a higher k_{ep} region, for example, tumor. For K^t, the result is more complicated because of the derivative polarity change for different k_{ep}